ACS APPLIED MATERIALS & INTERFACES

Research Article

www.acsami.org

Colloidal Synthesis of Cuprite (Cu_2O) Octahedral Nanocrystals and Their Electrochemical Lithiation

Andrea Paolella, Rosaria Brescia, Mirko Prato, Mauro Povia, Sergio Marras, Luca De Trizio, Andrea Falqui, Liberato Manna, and Chandramohan George*

Nanochemistry, Istituto Italiano di Tecnologia, Via Morego 30, 16163 Genova, Italy

Supporting Information

ABSTRACT: We report a facile colloidal route to prepare octahedral-shaped cuprite (Cu_2O) nanocrystals (NCs) of ~40 nm in size that exploits a new reduction pathway, i.e., the controlled reduction of a cupric ion by acetylacetonate directly to cuprite. Detailed structural, morphological, and chemical analyses were carried on the cuprite NCs. We also tested their electrochemical lithiation, using a combination of techniques (cyclic voltammetry, galvanostatic, and impedance spectroscopy), in view of their potential application as anodes for Li ion batteries. Along with these characterizations, the morphological, structural, and chemical analyses (via high-resolution electron microscopy, electron energy loss spectroscopy, and X-ray photoelectron spectroscopy) of the cycled Cu_2O NCs (in the lithiated stage, after ~50 cycles) demonstrate their partial conversion upon cycling. At this stage, most of the NCs had lost their octahedral shape and had evolved into multidomain particles and were eventually fragmented. Overall, the shape changes (upon cycling) did not appear to be concerted for all the NCs in the sample, suggesting that different subsets of NCs were characterized by different lithiation kinetics. We emphasize that a profound understanding of the lithiation reaction with NCs defined by a specific crystal habit is still essential to optimize nanoscale conversion reactions.

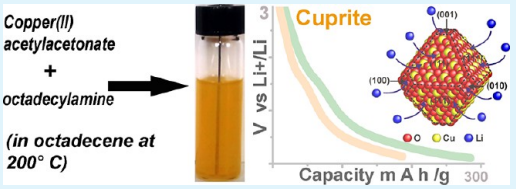

KEYWORDS: *copper oxide, colloidal nanocrystals, lithium ion batteries, anodes*

1. INTRODUCTION

Cuprous oxide, or cuprite (Cu_2O), is a naturally occurring ore of copper that finds applications in a wide range of fields. Cuprite has been in fact exploited in electronics and photovoltaics[1] (as it has a direct band gap of 2.17 eV), photo-induced water splitting,[2,3] catalysis,[4] gas sensors,[5] and Li-ion batteries,[6] which clearly demonstrates its importance among the transition metal oxides. Various laboratory scale synthetic routes to cuprite nanocrystals (NCs) have been reported to date, based on aqueous[7] and hydrothermal methods,[8] micro-emulsion,[9] polyol,[10] oxidation of colloidal Cu NCs,[11] high-temperature decomposition routes,[12] electro-deposition,[13] synthesis in supercritical water,[14] microemulsion γ-ray irradiation,[15] metallic copper oxidation,[16] reduction by hydrazine,[17] chemical vapor deposition (CVD),[18] and reduction by glucose.[19] Several studies also report on the electrochemical performance of cuprite in lithium ion batteries, on both micrometer[20] and sub-micrometer crystals.[21] It is well known that the lithiation of transition metal (such as Fe, Cu, Co, and Ni) oxides often involves a reversible conversion type of reaction, as reported by Tarascon and co-workers.[22] In the case of cuprite, the simplified cell reaction can be expressed as

$$Cu_2O + 2Li^+ + 2e^- \Leftrightarrow Li_2O + 2Cu^0$$

On the other hand, alloying/de-alloying and insertion/de-insertion (of Li^+ ions) processes were reported on other types of oxides, for example, SnO_2- and TiO_2-based nanostructures.[23] Recently, Luo et al. have shown that CuO-based nanostructures could be directly deposited on copper electrodes, exhibiting a significant capacity retention,[24] and similarly Barreca et al. have also shown that both CuO and Cu_2O could be deposited on Ti substrates[25] as electrode structures. Concerning the specific capacity values of cuprite (as reported from the literature), electrodeposited thin film[6] electrodes exhibited ~210−350 mAh/g, porous thin films with polystyrene[26] ~336−213 mAh/g, microsized cubic particles[20] ~390 mAh/g, and cuprite on Ti substrates[25] ~400−325 mA h/g (the theoretical capacity of cuprite is 374 mAh/g). Grugeon et al. investigated the electrochemical lithiation of micrometer and sub-micrometer cuprite particles (down to 100 nm).[21] In these systems, a complete conversion of the starting material into metallic nanoparticles (1−2 nm in size) dispersed in a Li_2O matrix was observed already upon the first discharge. Also, the smaller the particles, the larger was the capacity fading (however, based on comparing ~1 μm and 0.15 μm sized nearly spherical particles), which raises interesting questions regarding whether cuprite NCs smaller than 100 nm would bring any advantage in lithium ion batteries as anodes and how the lithiation reactions can affect the NCs in electrodes during a conversion reaction. Parallel to these issues, the study of how the NC shape[19,20,27] can influence the overall electrochemical properties has also

Received: January 30, 2013
Accepted: March 6, 2013
Published: March 6, 2013

   dx.doi.org/10.1021/am4004073 | ACS Appl. Mater. Interfaces 2013, 5, 2745−2751

triggered special interest in the conversion electrodes. Bao et al.[28] have shown for example that the (111) facets of cuprite NCs (which are well developed in octahedral-shaped particles) are much more reactive than the (100) facets in reactions involving H_2 or CO, but it is not clear if the same enhanced reactivity would be expected in electrochemical reactions with Li^+ ions. It is however well known that poor lithiation kinetics, poor capacity retention, and large voltage hysteresis (between the charge/discharge cycles) are still the main issues in electrochemical lithiation that exploit in particular a conversion/displacement reaction. Along these lines, it is interesting to study the lithiation properties of NCs with very specific size and shape, and this will help better explore different aspects of electrochemical lithiation including: (i) how the NC original shape/morphology evolves upon their lithiation; (ii) their reactivity with Li ions; (iii) the reversibility of conversion reactions. For these objectives, it is critical to maintain the original NC size and shape unaltered in the electrodes prior to cycling. We therefore made a composite in which the octahedral NCs could remain well dispersed and accessible to the electrolytes. In this way we avoided any possible sintering or coalescence of particles that may arise if they were directly deposited and annealed on substrates.

We report in this work a nonhydrolytic colloidal route to cuprite NCs, based on thermal decomposition of organometallic precursors in surfactants; i.e., Cu-acetylacetonate controlled the reduction of the cupric ion to cuprite. Such NCs were characterized by a uniform octahedral shape, narrow size distribution, and sizes around ∼40 nm. With the aim of elucidating electrochemical lithiation processes on these octahedral ∼40 nm cuprite NCs, we carefully monitored the formation of the lithiation products during the conversion processes and the morphological changes of the initial NCs. This was done via a combination of electrochemical techniques (cyclic voltammetry, galvanostatic, impedance spectroscopy) and by analyzing the cycled NCs via high-resolution transmission electron microscopy (HRTEM), electron energy loss spectroscopy (EELS), and X-ray photoelectron spectroscopy (XPS). Upon cycling, a progressively larger number of NCs were characterized by severe morphological changes, and many of them were eventually fragmented. The shape changes (upon conversion) did not occur uniformly for all the NCs in the sample, suggesting that different NCs presented different lithiation kinetics. Although the NC electrodes exhibited a lower capacity than what was previously reported in the literature, our study on ∼40 nm octahedral NCs will contribute to the understanding of lithiation reactions at the nanoscale and in particular of the lithiation reactions on NCs that are limited to a specific crystal plane (as in our case mainly the {111} ones).

2. EXPERIMENTAL SECTION

Materials. Octadecylamine (99.0%), oleylamine (70%), and 1-octadecene (95%) were purchased from Sigma Aldrich. Tetrachloroethylene was purchased from Sigma Aldrich >99% pure and anhydrous. Copper(II) acetylacetonate (purity >99.99%) was purchased from Strem. Toluene (anhydrous, analytical standard) and ethanol (anhydrous, analytical standard) were purchased from Carlo Erba. Cell components for coin type 2032 were purchased from Hohsen Corporation. Polypropylene microporous matrixes were purchased from Cellguard. Li metal foils were purchased from Goodfellow. Ethylene carbonate, diethyl carbonate, *N*-methyl-2-pyrrolidone, (poly)vinylidene difluoride, and carbon powder were purchased from Aldrich and Alfa Aesar. All the solvents used were thoroughly degassed.

Characterization Techniques. High-resolution scanning electron microscopy (HRSEM) investigations were carried out using a JEOL JSM 7500FA instrument, equipped with a cold field emission gun (FEG), operating at 5 kV accelerating voltage. Energy-dispersive X-ray spectroscopy (EDX) was performed using a JEOL Hyper Nine Energy Si(Li) EDX Detector EX-64195JNH (10 mm^2 effective area of detecting device, ultrathin window for detection of elements from Be to U, energy resolution (FWHM): 133 eV for Mn Kα X-rays). Bright-field transmission electron microscopy (BF-TEM) images and selected area electron diffraction (SAED) patterns were recorded on a JEOL JEM-1011 microscope, equipped with a thermionic W source and operated at 100 kV. HRTEM, energy filtered TEM (EFTEM), EELS, and scanning TEM (STEM) analyses—the latter in high angle annular dark field (HAADF) geometry—were performed with a JEOL JEM-2200FS microscope working at an accelerating voltage of 200 kV, equipped with a Schottky FEG, a CEOS spherical aberration corrector of the objective lens allowing us to reach a spatial resolution of 0.9 Å, and an in-column Omega filter. Chemical compositions were determined for several particles by quantification of the EEL spectra, using the Cu-L_{23} and the O−K edges. The spectra used for quantification were recorded in diffraction mode using a 5.1 mrad collection semiangle and with a convergence semiangle of 2.5 mrad and with an energy dispersion of 0.4 eV/channel. For both core loss edges the quantification was done by subtracting a power law background, by deconvoluting the low loss spectrum for the corresponding region, and by assuming a hydrogenic model for the cross section.[29] In addition, the energy loss near edge structure (ELNES) in the EEL spectra acquired from the particles was compared to the one observed for a Cu_2O standard powder sample (Sigma-Aldrich, purity >99.99%). The EELS near-edge structure was compared for spectra acquired with a 0.2 eV/channel energy resolution. EFTEM elemental maps were acquired for oxygen (K edge at 532 eV, 30 eV slit width) and Cu (L_{23} edge at 931 eV, 50 eV slit width). All the samples analyzed by TEM were prepared by dropcasting a solution of NCs onto copper grids covered with an ultrathin carbon film on top of a lacey carbon film. The samples for EELS quantification were instead deposited onto holey carbon films. The specimens were prepared under nitrogen and transferred into the microscope using a vacuum transfer holder to avoid air exposure prior to investigation.

X-ray diffraction (XRD) measurements were obtained using a Smartlab 9 kW Rigaku diffractometer equipped with a copper rotating anode. The X-ray source was operated at 40 kV and 150 mA. A Göbel mirror was used to obtain a parallel beam and to suppress Cu Kβ radiation (1.392 Å). The 2 theta/omega scan was performed with two radiations, Cu Kα1 (1.544 Å) and Cu Kα2 (1.541 Å), with a step of 0.05° (2 theta) and with a scan speed of 3°/min. The specimens for XRD measurements were prepared in a glovebox, under nitrogen atmosphere, and inserted inside the DHS900 sample holder (Anton Paar), allowing us to transfer the samples to the diffractometer in inert atmosphere and to perform the measurements under vacuum condition. In this way the sample was never exposed to the air. The software PDXL by Rigaku was used for qualitative analysis.

XPS and X-ray induced Auger electron spectroscopy (XAES) measurements were performed on a Kratos Axis Ultra DLD spectrometer, using a monochromatized Al Kα source operating at 15 kV and 20 mA. Samples were prepared by drop casting a solution of NCs onto highly oriented pyrolytic graphite (HOPG) substrates under inert atmosphere, in a glovebox, and were then transferred to the XPS analysis chamber through a transfer vessel, to avoid any air exposure. Wide scans were acquired at an analyzer pass energy of 160 eV. High-resolution narrow scans on both as-synthesized and lithiated samples were performed at constant pass energy of 10 eV and steps of 0.1 eV. Kratos charge neutralizer system was used on all the samples for charge compensation. The binding energy (BE) scale was internally referenced to the C 1s peak (BE for C−C = 284.6 eV). The photoelectrons were detected at a take-off angle $\Phi = 0°$ with respect to the surface normal. The pressure in the analysis chamber was

maintained below 5×10^{-9} Torr for data acquisition. The data were converted to VAMAS format and processed using CasaXPS software, version 2.3.15.

Optical absorption measurements on NC solutions were carried out using a Varian Cary 5000 UV-vis-NIR spectrophotometer. The solvent used was tetrachloroethylene in all the optical absorption measurements. Thermogravimetric analysis (TGA) was performed on dried cuprite NC samples (sample gas: air 60.0 mL/min) using a TGA Q500 instrument.

All the electrochemical measurements were carried out using a PARSTAT2273 potentiostat/galvanostat. In an argon-filled glovebox, Cu_2O NCs were washed several times with a 1:1 mixture of ethanol and toluene and finally precipitated, and the precipitate was dried. The dried powder was mixed with carbon and polyvinylidene difluoride (PVDF) in *N*-methyl-2-pyrrolidone (degassed), such that the weight fraction of NCs in the resulting mixture was 85%. The mixture was stirred well to obtain a homogeneous slurry. Then the NC slurry was coated onto the current collector and dried at 120 °C for 48 h. To prepare batteries, 2032 coin type cells were assembled in which the current collector coated with the Cu_2O NC slurry served as one electrode, while a Li metal disk served as both reference and counter electrode. The electrolyte was made by a solution of 1 M lithium hexafluorophosphate in 1:1 ethylene carbonate and diethyl carbonate, and layers of polypropylene were used to separate the electrodes. The cycled NCs were scratched from the electrodes upon opening the cells in the glovebox. The cycled NCs were washed and dispersed in pure toluene for further characterizations.

3. RESULTS AND DISCUSSION

Synthesis of Colloidal Cu_2O NCs. In a typical synthesis of cuprite NCs, copper(II) acetylacetonate (0.130 g, 0.5 mmol) was mixed with octadecylamine (ODA, 0.80 g, 3 mmol) and 1-octadecene (ODE, 10 mL), and the resulting solution was pumped to vacuum at 120 °C and then placed under N_2 for 10 min. The color of this initial solution of reactants, at room temperature, was blue, which is indicative of the presence of cupric ions. When the temperature reached 120 °C, the solution became dark green (most likely due to the formation of cuprous ions) and then yellow as soon as it reached 200 °C. Well-defined octahedral cuprite NCs were observed after keeping the solution at this temperature for 20−30 min, after which the synthesis was stopped. Figure 1(a,b) reports SEM and BF-TEM images of such Cu_2O NCs, having an average edge length of 41(±7) nm. Elemental mapping of a group of NCs, acquired by EFTEM, proved the homogeneous distribution of oxygen and copper in the NCs (Figure 1e). Compositional analysis of a much larger group of particles, by HRSEM-EDX, is reported in the Supporting Information.[30]

XRD patterns of the NCs evidenced a good match with cuprite (cubic Cu_2O, a = 4.2696 Å, space group *Pn*-3*m*, Figure 2a). The cuprite phase was also supported by HRTEM analyses of individual NCs (Figure 1c,d). The optical absorption of a solution of cuprite NCs, in the UV−VIS−NIR, is reported in Figure 2b: an optical band gap of ∼2.3 eV was estimated for the NCs (see the corresponding Tauc plot in the inset of Figure 2b). Results of XPS and XAES are shown in Figure 2c,d. XPS Cu $2p_{3/2}$ and Cu $2p_{1/2}$ peaks were found at binding energy (BE) values of 932.0 and 951.8 eV, respectively. The position of the Cu $2p_{3/2}$ peak (Figure 2c), together with that of the Cu LMM Auger peak (Figure 2d) at a kinetic energy of 917.1 eV (corresponding to an Auger parameter of 1849.1 eV),[31] was consistent with copper(I) oxide.[11] The near-edge structure of the EEL spectra (Figure 1f), in the regions of the O K and the Cu L core-loss edges, recorded from several NCs, showed complete agreement with that of a reference Cu_2O powder, in terms of energy onset position, asymmetry, and intensity ratio of the Cu L_3 to Cu L_2 peaks.[32] EEL spectra allowed also the determination of the Cu/O atomic ratio, which was equal to 2.2 ± 0.2.

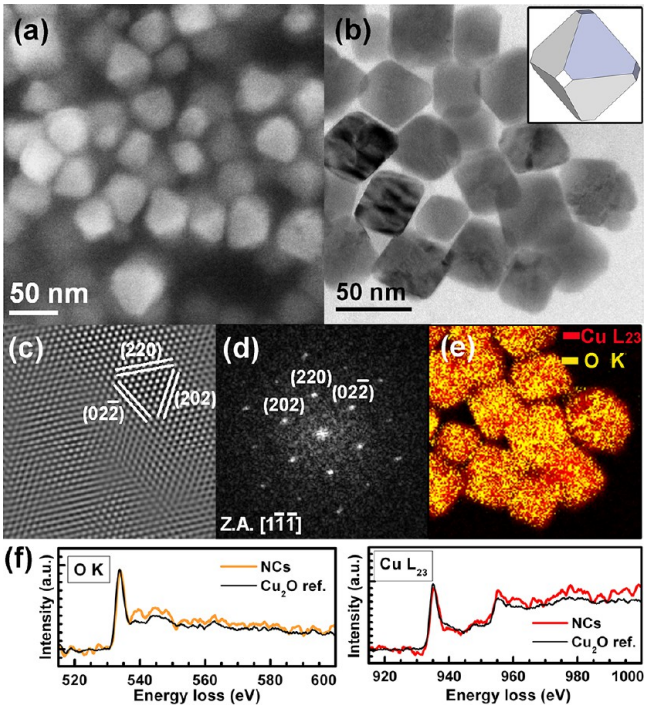

Figure 1. (a) SEM and (b) bright-field (BF) TEM images of the Cu_2O NCs, evidencing their slightly truncated octahedral shape; (c) Fourier-filtered HRTEM image of a selected region of one NC and (d) corresponding Fourier transform (FT), with the pattern of cuprite; (e) combined EFTEM elemental maps of O (yellow) and Cu (red) from the same group of NCs in (a); (f) EEL spectra, in the regions of the O K and Cu L_{23} edges, of a group of NCs, showing the good match of the near-edge structures with the Cu_2O reference.

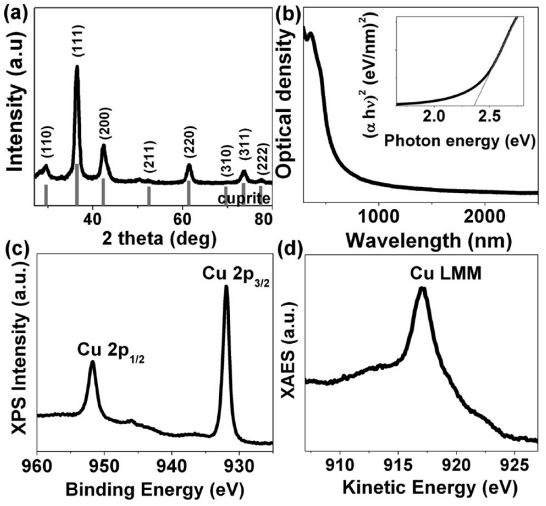

Figure 2. (a) XRD pattern acquired on the NC sample, compared with the database card 00-005-0667 (cuprite, cell parameter a = 4.2696 Å, space group *Pn*-3*m* (224)); (b) UV-VIS-NIR spectrum, inset in (b) reports the Tauc plot for the optical band gap; (c,d) Cu 2p and Cu LMM Auger peaks recorded via XPS and XAES, respectively.

TGA analysis on the NCs evidenced a first weight loss at ∼150° C after isothermal heating, which could be due to the

dx.doi.org/10.1021/am4004073 | ACS Appl. Mater. Interfaces 2013, 5, 2745−2751

solvent evaporation, then a gradual loss until ~300 °C, which could be due to the surfactant removal from the NC surface.[30]

In the synthesis, ODA acted both as a surfactant and as a regulator of the reduction of Cu^{2+}: when Cu(II) acetylacetonate was heated in 1-octadecene at 200°C in the absence of ODA, mostly submicrometer sized metallic copper particles were found. Therefore, while acetylacetonate was the main agent responsible for the reduction of cupric ions, this reduction, in the absence of ODA, did not stop at cuprous ions but in part went further to Cu(0) (the reducing ability of acetylacetone, i.e., the conjugated acid of acetylacetonate, was already demonstrated by Tollan et al.[33]). On the other hand, when the concentration of ODA was increased considerably in solution (~10 times), in addition to obtaining smaller NCs (average size: 5−10 nm), which is understandable given the role of ODA as surfactant, also a fraction of metal copper NCs were formed. Therefore, when present at high concentrations, ODA competed with acetylacetonate in the reduction of Cu^{2+}. We also tested syntheses using copper(II) acetate instead of copper(II) acetylacetonate, which yielded only metallic copper NCs. This indicates that acetate is a stronger reducing agent than acetylacetonate, and its reducing ability cannot be regulated by the alkylamine. Additional tests (and control experiments) are found in the Supporting Information.[30] The length of the alkyl chain in the amine was critical for the synthesis of octahedral particles with narrow size distributions. For example, when using octylamine instead of ODA, irregularly shaped cuprite NCs with broad size distributions were formed. Replacing ODA with other surfactants, for example, oleic acid, yielded only micrometer and submicrometer particles of metallic copper. It appears then that an alkylamine of suitable chain length is required to stabilize the reaction towards the sole formation of cuprite NCs with specific size and shape and narrow size distribution. The octahedral habit for these NCs can be rationalized by the generally high thermodynamic stability of the nonpolar Cu_2O (111) facets over the (100) and (110) ones,[34] which most likely is further enhanced by the passivation with ODA.

Electrochemical Lithiation. Electrodes were then prepared by coating current collectors with a homogeneous slurry containing the NCs. TEM analysis of the slurry showed a uniform distribution of the particles (NCs) throughout the sample.[30] Figure 3a reports typical discharge curves from the Cu_2O NC electrodes in a half cell with a Li metal counter-electrode at a current density of 1 mA. After a fast sloping voltage plateau at about 1.8−1.5 V (corresponding to the first lithiation step of cuprite NCs vs Li/Li^+), there was another fair voltage plateau at about 0.7−0.5 V ($Cu_2O \rightarrow Cu$),[26] and the last plateau was below 0.5 V, where the deep lithiation begins and the electrolyte reduction leads to the formation of a solid electrolyte interface (SEI). The three voltage plateaus indicate that the process of Li^+ ion intake occurs in steps. In the first cycle, these voltage plateaus together could deliver a capacity of 280 mA h g^{-1} at a current density of 1 mA (we recall here that the theoretical capacity of Cu_2O is ~374 mA h g^{-1}),[26] from which about 60% was retained in the second cycle. The irreversible loss of capacity is typically attributed to the formation of a SEI,[35] with the subsequent consumption of Li^+ ions from the electrolyte. In the successive discharge cycles, the capacity gradually faded but stabilized at about 100 mAh/g from the 40th cycle (and the 50th cycle is also reported in Figure 3b). This can be seen in the inset of Figure 3a where the discharge capacity versus number of cycles is reported.

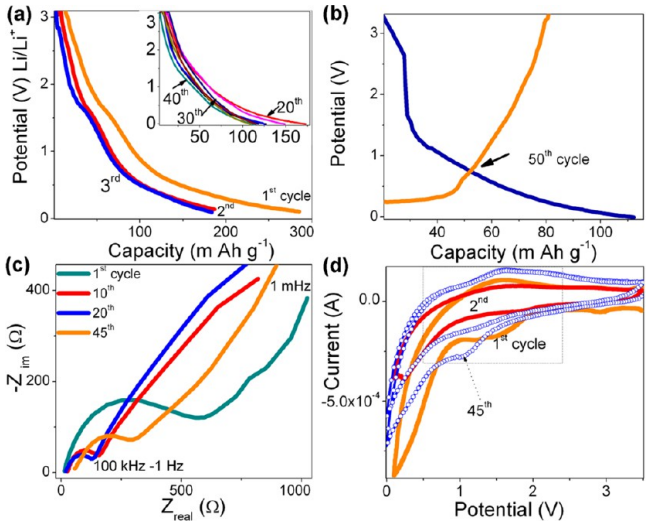

Figure 3. (a) First three discharge curves from the Cu_2O NC electrode at 1 mA (the inset graph shows discharge curves for later selected cycles). (b) The charge/discharge in the 50th cycle; (c) Nyquist plot (for impedance curves) of a typical Cu_2O NC electrode upon cycling; (d) CV response of the Cu_2O NC electrode at 5 mV/s (first and second cycle), the dotted CV curves from after 45 cycles.

Nevertheless, the NCs used in the cells with Li exhibited overall a low capacity.

To better understand the lithiation/delithiation processes at the electrode/electrolyte interface, electrochemical impedance spectroscopy (EIS) was performed on the cells in the lithiated state. Figure 3c reports the Nyquist plot of the lithiated Cu_2O NCs, where the complex impedance curve represents various interfacial processes at the electrode/electrolyte interface,[36] which appear as a semicircle in the high frequency region and a linear portion in the low frequency domain. In other words, in the high frequency region (100−1 kHz), the intercept on the Z_{real} axis corresponds to the electrolyte resistance (R_e). The depressed semicircle in the middle high frequency region is due to the presence of SEI (R_{sf}) combined with the charge-transfer resistance (R_{ct}) for the transfer of Li^+ ions across the SEI to the electrode bulk. In the low frequency region (from 1 Hz to 1mHz) the spike-like line (a resistive component associated with Warburg impedance (Z_w)) at a slope of 45° is a signature of the Li^+ ion diffusion in solids. The onset of conversion processes associated with Li^+ ion insertion kinetics could be observed by the reduction of the initially broad semicircle upon cycling. The variations of semicircle diameter (from which the R_{ct} derived)[37] could also refer to the result of fragmentation of the NCs in the successive conversion processes, which modifies the electronic conductive paths in NC electrodes. Besides, it is also plausible that while the NCs are being lithiated and delithiated (upon cycling) the ionic diffusion[36] on those NCs fluctuates due to the varied amount of Li^+ ions in the lithiated phases of the NCs.

We additionally performed cyclic voltammetry (CV) on the electrodes at a scan rate of 5 mV/s (Figure 3d). In the first cycle, the lithiation at the surface level started at about 1.6 V, leading to a prominent peak at 1.5 V. After this first insertion potential, the broad shoulders appeared in steps at 1.0 and 0.6 V for the second step of lithiation. At potentials below 0.5 V, a strong reduction current indicated the occurrence of several possible processes, such as the onset of a deep discharge zone, the passivation of the NC surface due to the formation of the

SEI layer, the extrusion of copper ions from NCs, and the formation of lithium oxides. The buildup of an SEI on the NCs (as a result of the reduction of electrolytes near the surface of the particles during the initial discharges)[38] could be seen from the CV data (Figure 3d) in the potential range around 0.3 V as a broad sloping peak. Indications of such surface coating on the NC surface can be inferred from HRTEM (Figure 5a). On the reverse scan, the oxidation process was evidenced by two broad shoulders at about 1.5 and 2.6 V, which were attributed to the decomposition of the lithium oxides, SEI phases,[26] and partially lithiated phases. All these processes were evident as voltage plateaus in the discharge process (Figure 3a). Along the cycles (for instance after the 45th cycle), the recorded CV (Figure 3d, dotted curves) already revealed that the peak potential was slightly shifted in the forward scan (insertion) due to conversion effect, which suggests that several NCs in the electrode could have been chemically altered.

To study the structural evolution of the Cu_2O NCs after cycling, we first carefully performed the ex situ BF-TEM survey analysis (for cycles terminated in the deep lithiation stage) as reported in Figure 4a,b and then performed a detailed HRTEM

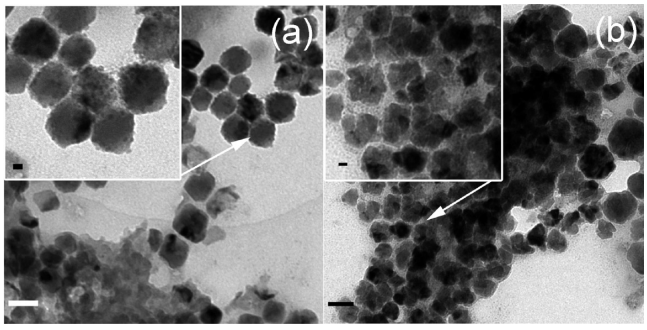

Figure 4. Representative BF-TEM survey image showing the Cu_2O NCs after different cycle number, stopped in the lithiation stage: (a) ~40 and (b) ~50, respectively, indicating the morphological changes on the NCs. The scale bars correspond to 50 nm in each panel and 10 nm in each inset.

and EELS investigation. The overall results suggest that in the early cycles the products of such a conversion process might be extremely small, below the detection limit of our characterization techniques. Moreover, the diffraction features from such tiny conversion products, in case they are arranged in crystalline structures, might be negligible with respect to those of the unconverted Cu_2O NCs, in XRD and electron diffraction analyses.[30] After about 40 cycles, instead, some of the NCs were severely damaged, and several ≈1 nm sized crystalline grains started to appear (Figure 4a, see also Figures S11 and S12 of the Supporting Information[30]), probably resulting from fragmentation of the cuprite NCs. HRTEM analyses allowed us to identify some of them as metallic copper and Li_2O.[30] Still, at this stage, most of the NCs had preserved their pristine octahedral shape and cuprite structure (Figure 5a–c). Similar observations were reported on lithiation of hollow iron oxide nanocrystals[39] by Koo et al., showing that the nanocrystals were able to retain their overall shape. On the other hand, in cuprite no evidence of lithiation mechanisms other than conversion has been reported to date.

One plausible explanation of why the NCs did not change much even after many cycles is that they were characterized by a poor lithiation kinetics, and most likely this is the reason why

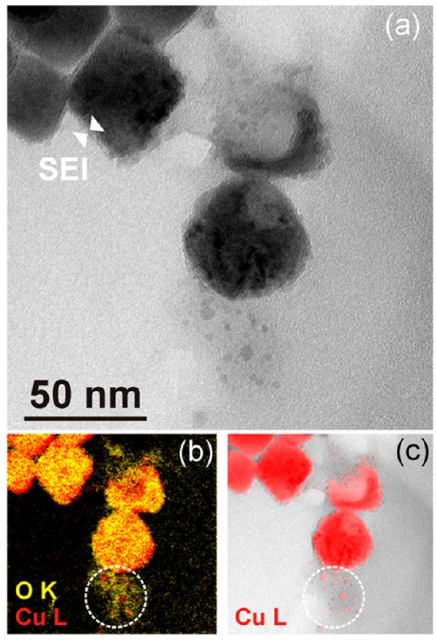

Figure 5. Representative TEM images of cuprite NCs after 40 cycles. (a) BF-TEM image of an area showing nanometer-sized NCs besides the large octahedrons, the latter more or less damaged; (b,c) combinations of the EFTEM elemental map of Cu (red) with (b) EFTEM map of O (yellow) and (c) BF-TEM image (gray scale) of the same region, showing that Cu is contained in some of the tiny particles.

their overall capacity was low. This in turn might be due to various factors, related for example to a different surface termination or passivation of these NCs with respect to cuprite particles of previous works. Furthermore, it is conceivable that at this stage the NCs exhibited progressively poorer interparticle connectivity and loss of electrical pathways,[40] which indeed would explain a fading in the capacity (the corresponding charge/discharge cycles of the cuprite samples are reported in the Supporting Information, S13).[30] The fraction of the severely damaged and eventually the fragmentation of NCs increased considerably after 50 cycles (Figures 4b and 6). At this stage, the cycling stress apparently caused cracks on all the NCs, such that they were transformed into multidomain particles (Figure 6b). HRTEM investigations indicated that still the larger NCs had retained the cuprite structure.[30] Many of the smaller particles (≤10 nm) that populated the sample at this stage exhibited a crystalline structure (Figure 6d, e, g–l) and were ascribed to a variety of phases. Besides tiny metallic Cu NCs (Figure 6g,h), incomplete conversion products were identified, such as nonstoichiometric Cu oxide (orthorhombic Cu_8O)[41] (Figure 6d–e) and mixed Cu–Li oxide (tetragonal LiCuO)[42] NCs (Figure 5i–l). In agreement with HRTEM, XPS analysis of those NCs also confirmed the presence of several Cu compounds. Cu peaks in fact were broader than those of the starting NCs, and no satellites typical of Cu(II) species appeared,[30] as expected in the case of lithiated samples. The detection by HRTEM of very small domains either poorly structured or with structure different from that of the large cuprite NCs was not straightforward. Therefore, it cannot be ruled out that such nanometer-sized domains containing Li or metallic Cu or mixed Li–Cu oxides are also present on the surface and/or within the bulk of the larger NCs. Indeed, a low Li content was

dx.doi.org/10.1021/am4004073 | ACS Appl. Mater. Interfaces 2013, 5, 2745–2751

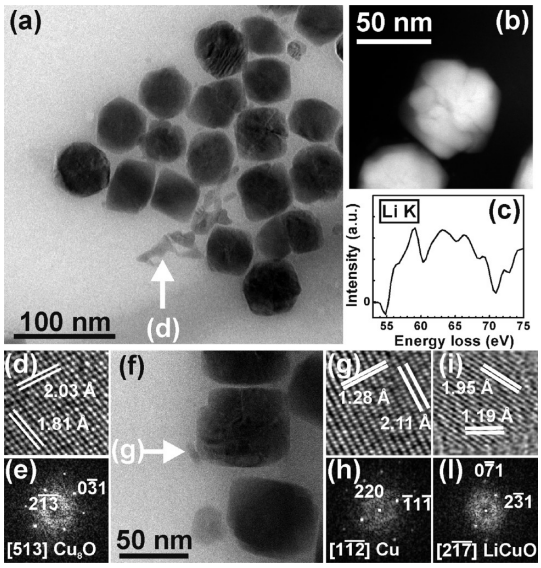

Figure 6. Representative HRTEM and EELS results obtained on the ~50 times cycled sample in the lithiated stage. (a) Overview BF-TEM image of a group of NCs, indicating the presence of smaller particles besides the ~40 nm ones; (b) STEM-HAADF image of an individual NC, clearly showing cracks within its volume; (c) EEL spectrum collected over a group of ~10 large NCs in the region of the Li K edge; (d,e) HRTEM image and corresponding FT of a region of the filament-like feature seen in (a), from which it can be concluded that this feature was made of orthorhombic Cu_8O (a = 5.47 Å, b = 6.02 Å, c = 9.34 Å). (f) BF-TEM image of a region where smaller particles are visible besides large cuprite NCs; (g) HRTEM image and (h) relative FT of the particle indicated with an arrow in (f), which shows the structure of metallic Cu. (i–l) HRTEM image and FT of a ~4 nm diameter particle. The FT is compatible with tetragonal LiCuO (a = b = 8.514 Å, c = 3.809 Å).

detected by EELS in an area including ~10 of the larger NCs, showing a weak signal corresponding to the Li K core-loss edge at ~55 eV (Figure 6c).

4. CONCLUSION

We have reported a facile synthesis route to prepare octahedral shaped cuprite (Cu_2O) NCs and presented their extensive characterizations. The electrochemical lithiation properties of the NCs as anodes (in Li ion batteries) were studied by galvanostatic, cyclic voltammetry, and electrochemical impedance spectroscopy. We also followed the morpho-structural and chemical modifications of cuprite NCs upon cycling via ex situ HRTEM, EELS, and XPS (on lithiated NCs). After prolonged cycling, in the lithiated state, most of the NCs showed severe morphological changes evidencing their conversion reaction. However, it is interesting to notice that some of the initial NCs were able to preserve their octahedral shape even after 40–50 cycles, which clearly points to poor lithiation kinetics. Additionally, different subsets of NCs appeared to be characterized by different lithiation kinetics. Clearly, it would be interesting to compare the results on the present octahedral-shaped cuprite NCs with those of cuprite NCs of other morphologies, for example, nanocubes exposing (001) facets, in a similar range of sizes, to study in depth the NC morphology-dependent lithiation reactions. However, so far our synthesis approaches did not allow us to access such shapes, and work is in progress in our group to try to tackle this issue. A possible future implementation of the present NCs as anode materials could be their integration with suitable elastic buffers (for example graphene layers) or a formation of percolating networks of NCs directly on metal substrates. At present, studies on interfacing the NCs with suitable polymeric nanostructures in combination with efficient elastic buffers are underway in our group.

■ ASSOCIATED CONTENT

Supporting Information

Control synthesis experiments and additional data on TEM, XRD, TGA, HRSEM-EDX, and XPS analysis. This material is available free of charge via the Internet at http://pubs.acs.org.

■ AUTHOR INFORMATION

Corresponding Author

*Tel.: +39 010 71781 979. E-mail: chandramohan.george@iit.it.

Notes

The authors declare no competing financial interest.

■ ACKNOWLEDGMENTS

The authors acknowledge financial support from European Union through the FP7 starting ERC grant NANO-ARCH (contract #240111) and the Italian FIRB grant (contract #RBAP115AYN). Dr. Tania Montanari is acknowledged for help with TGA analysis.

■ REFERENCES

(1) Lee, Y. S.; Winkler, M. T.; Siah, S. C.; Brandt, R.; Buonassisi, T. *Appl. Phys. Lett.* **2011**, *98*, 192115.
(2) de Jongh, P. E.; Vanmaekelbergh, D.; Kelly, J. J. *Chem. Commun.* **1999**, 1069–1070.
(3) Barreca, D.; Carraro, G.; Gombac, V.; Gasparotto, A.; Maccato, C.; Fornasiero, P.; Tondello, E. *Adv. Funct. Mater.* **2011**, *21*, 2611–2623.
(4) Bordiga, S.; Paze, C.; Berlier, G.; Scarano, D.; Spoto, G.; Zecchina, A.; Lamberti, C. *Catal. Today* **2001**, *70*, 91–105.
(5) Barreca, D.; Comini, E.; Gasparotto, A.; Maccato, C.; Sada, C.; Sberveglieri, G.; Tondello, E. *Sens. Actuators, B* **2009**, *141*, 270–275.
(6) Morales, J.; Sanchez, L.; Bijani, S.; Martinez, L.; Gabas, M.; Ramos-Barrado, J. R. *Electrochem. Solid State Lett.* **2005**, *8*, A159–A162.
(7) Gou, L. F.; Murphy, C. J. *Nano Lett.* **2003**, *3*, 231–234.
(8) Tan, Y.; Xue, X.; Peng, Q.; Zhao, H.; Wang, T.; Li, Y. *Nano Lett.* **2007**, *7*, 3723–3728.
(9) Dodoo-Arhin, D.; Leoni, M.; Scardi, P.; Garnier, E.; Mittiga, A. *Mater. Chem. Phys.* **2010**, *122*, 602–608.
(10) Kim, M. H.; Lim, B.; Lee, E. P.; Xia, Y. *J. Mater. Chem.* **2008**, *18*, 4069–4073.
(11) Yin, M.; Wu, C. K.; Lou, Y. B.; Burda, C.; Koberstein, J. T.; Zhu, Y. M.; O'Brien, S. *J. Am. Chem. Soc.* **2005**, *127*, 9506–9511.
(12) Yao, K. X.; Yin, X. M.; Wang, T. H.; Zeng, H. C. *J. Am. Chem. Soc.* **2010**, *132*, 6131–6144.
(13) Siegfried, M. J.; Choi, K. S. *Adv. Mater.* **2004**, *16*, 1743–1746.
(14) Ziegler, K. J.; Doty, R. C.; Johnston, K. P.; Korgel, B. A. *J. Am. Chem. Soc.* **2001**, *123*, 7797–7803.
(15) He, P.; Shen, X. H.; Gao, H. C. *J. Colloid Interface Sci.* **2005**, *284*, 510–515.
(16) Ng, C. H. B.; Fan, W. Y. *J. Phys. Chem. B* **2006**, *110*, 20801–20807.
(17) Xu, H.; Wang, W.; Zhu, W. *J. Phys. Chem. B* **2006**, *110*, 13829–13834.
(18) Barreca, D.; Gasparotto, A.; Maccato, C.; Tondello, E.; Lebedev, O. I.; Van Tendeloo, G. *Cryst. Growth Des.* **2009**, *9*, 2470–2480.
(19) Gao, X. P.; Bao, J. L.; Pan, G. L.; Zhu, H. Y.; Huang, P. X.; Wu, F.; Song, D. Y. *J. Phys. Chem. B* **2004**, *108*, 5547–5551.

(20) Zhang, C. Q.; Tu, J. P.; Huang, X. H.; Yuan, Y. F.; Chen, X. T.; Mao, F. *J. Alloys Compd.* **2007**, *441*, 52−56.
(21) Grugeon, S.; Laruelle, S.; Herrera-Urbina, R.; Dupont, L.; Poizot, P.; Tarascon, J. M. *J. Electrochem. Soc.* **2001**, *148*, A285−A292.
(22) Poizot, P.; Laruelle, S.; Grugeon, S.; Dupont, L.; Tarascon, J. M. *Nature* **2000**, *407*, 496−499.
(23) Wu, H. B.; Chen, J. S.; Hng, H. H.; Wen David Lou, X. *Nanoscale* **2012**, *4*, 2526−2542.
(24) Wang, Z.; Su, F.; Madhavi, S.; Lou, X. W. *Nanoscale* **2011**, *3*, 1618−1623.
(25) Barreca, D.; Carraro, G.; Gasparotto, A.; Maccato, C.; Cruz-Yusta, M.; Gomez-Camer, J. L.; Morales, J.; Sada, C.; Sanchez, L. *ACS Appl. Mater. Interfaces* **2012**, *4*, 3610−3619.
(26) Xiang, J. Y.; Wang, X. L.; Xia, X. H.; Zhang, L.; Zhou, Y.; Shi, S. J.; Tu, J. P. *Electrochim. Acta* **2010**, *55*, 4921−4925.
(27) Park, J. C.; Kim, J.; Kwon, H.; Song, H. *Adv. Mater.* **2009**, *21*, 803−807.
(28) Bao, H.; Zhang, W.; Shang, D.; Hua, Q.; Ma, Y.; Jiang, Z.; Yang, J.; Huang, W. *J. Phys. Chem. C* **2010**, *114*, 6676−6680.
(29) Egerton, R. F. *Electron Energy-Loss Spectroscopy in the Electron Microscope*, 2nd ed.; Plenum Press: New York, 1996.
(30) See Supporting Information for additional details.
(31) Gaarenstroom, S. W.; Winograd, N. *J. Chem. Phys.* **1977**, *67*, 3500−3506.
(32) Ngantcha, J. P.; Gerland, M.; Kihn, Y.; Riviere, A. *Eur. Phys. J. Appl. Phys.* **2005**, *29*, 83−89.
(33) Tollan, C. M.; Echeberria, J.; Marcilla, R.; Pomposo, J. A.; Mecerreyes, D. *J. Nanopart. Res.* **2009**, *11*, 1241−1245.
(34) Zheng, Z.; Huang, B.; Wang, Z.; Guo, M.; Qin, X.; Zhang, X.; Wang, P.; Dai, Y. *J. Phys. Chem. C* **2009**, *113*, 14448−14453.
(35) Chung, K. Y.; Yoon, W.-S.; Kim, K.-B.; Cho, B.-W.; Yang, X.-Q. *J. Appl. Electrochem.* **2011**, *41*, 1295−1299.
(36) Dilena, E.; Dorfs, D.; George, C.; Miszta, K.; Povia, M.; Genovese, A.; Casu, A.; Prato, M.; Manna, L. *J. Mater. Chem.* **2012**, *22*, 13023−13031.
(37) Kang, J.-G.; Ko, Y.-D.; Park, J.-G.; Kim, D.-W. *Nanoscale Res. Lett.* **2008**, *3*, 390−394.
(38) Zhang, S. S. *J. Power Sources* **2006**, *162*, 1379−1394.
(39) Koo, B.; Xiong, H.; Slater, M. D.; Prakapenka, V. B.; Baasubramanian, M.; Podsiadlo, P.; Johnson, C. S.; Rajh, T.; Shevchenko, E. V. *Nano Lett.* **2012**, *12*, 2429−2435.
(40) Song, M.-K.; Park, S.; Alamgir, F. M.; Cho, J.; Liu, M. *Mater. Sci. Eng., R* **2011**, *72*, 203−252.
(41) Guan, R.; Hashimoto, H.; Kuo, K. H. *Acta Crystallogr., Sect. B: Struct. Sci.* **1984**, *40*, 560−566.
(42) Migeon, H. N.; Zanne, M.; Gleitzer, C. *J. Solid State Chem.* **1976**, *16*, 325−330.